# UC Davis

## UC Davis Previously Published Works


### Title

Mechanism of Cr(VI) removal by magnetic greigite/biochar composites


### Permalink

https://escholarship.org/uc/item/9ph9g5vw



### Authors

Wang, Xuedong
Xu, Jin
Liu, Jia
et al.



### Publication Date

2020

### DOI

10.1016/j.scitotenv.2019.134414

Peer reviewed



eScholarship.org Powered by the California Digital Library
University of California

Science of the Total Environment (2020) 134414

Contents lists available at ScienceDirect

Science of the Total Environment

journal homepage: www.elsevier.com/locate/scitotenv

# Mechanism of Cr(VI) removal by magnetic greigite/biochar composites

Xuedong Wang [a,1], Jin Xu [a,1], Jia Liu [a], Jun Liu [a], Fang Xia [a], Cuicui Wang [a], Randy A. Dahlgren [a,b], Wei Liu [a,*]

[a] Zhejiang Provincial Key Laboratory of Watershed Science and Health, Southern Zhejiang Water Research Institute, College of Public Health and Management, Wenzhou Medical University, Wenzhou 325035, People's Republic of China
[b] Department of Land, Air and Water Resources, University of California, Davis, CA 95616, United States

## HIGHLIGHTS

- Magnetic greigite/biochar composites (MGBs) were synthesized by a solvothermal method.
- Cr(VI) was efficiently adsorbed and reduced on MGBs.
- Cr(VI) removal efficiency depended on the $Fe_3S_4$ amounts loaded on MGBs.
- Fe(II) dissolved from MGBs played a crucial role in Cr(VI) removal.
- Carbon-centered PFRs on MGBs promoted the surface Fe(III)/Fe(II) cycle.

## GRAPHICAL ABSTRACT

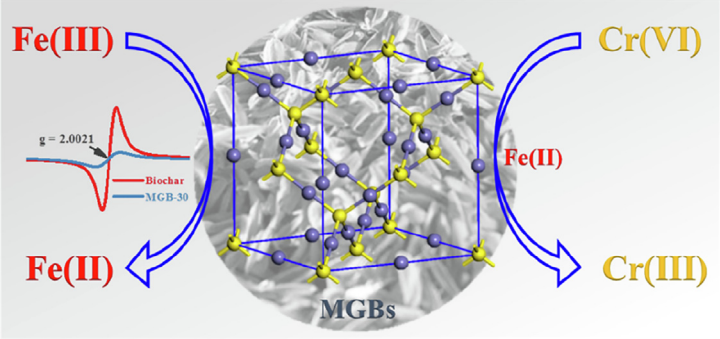


## ARTICLE INFO

*Article history:*
Received 8 July 2019
Received in revised form 10 September 2019
Accepted 10 September 2019
Available online 12 September 2019

Editor: Daniel CW Tsang

*Keywords:*
Greigite
Biochar
Fe(III)/Fe(II) cycling
Redox
Cr(VI)

## ABSTRACT

This study synthesized magnetic greigite/biochar composites (MGBs) by a solvothermal method and tested their ability to remove Cr(VI) from heavy metal-polluted wastewater. X-ray diffraction (XRD), Fourier transformed infrared spectrometry (FT-IR) and scanning electron microscopy (SEM) revealed that magnetic greigite ($Fe_3S_4$) flakes were aggregated and anchored to the biochar surface, resulting in more active sites than pristine biochar. Maximum Cr removal efficiency and capacity of MGB-30 (greigite/biochar = 30%) at an initial Cr(VI) concentration of 20 mg/L were 93% and 23.25 mg/g, respectively. A pseudo-first-order kinetic model was determined for the Cr(VI) removal process and the Cr(VI) removal rate constants were highly dependent on the mass ratios of $Fe_3S_4$ loaded on biochar, initial MGB and Cr(VI) concentrations and solution pH. X-ray photoelectron spectroscopy (XPS) and flame atomic absorption spectrometric (FAAS) analysis demonstrated that Cr(VI) was preferentially adsorbed on MGBs and subsequently reduced to Cr(III) by MGBs. Electron paramagnetic resonance (EPR) spectroscopy and iron redox transformations revealed that the Cr(VI) removal enhancement was attributed to efficient surface Fe(III)/Fe(II) cycling via electron transfer with the persistent free radicals (PFRs) of biochar. These novel findings provide new insights into the Fe(III)/Fe(II) cycle induced by biochar and the prospects of using magnetic greigite/biochar composites for remediation of Cr(VI)-rich wastewaters.

© 2019 Elsevier B.V. All rights reserved.

## 1. Introduction

Chromium, a commonly occurring heavy metal derived from textile dying, wood preserving, tanning, and galvanic processing, is frequently detected at elevated levels in wastewater, hazardous industrial waste, and polluted soil (Kimbrough et al., 1999; Rai

* Corresponding author.
*E-mail address:* liu_wei@wmu.edu.cn (W. Liu).
[1] These authors should be considered co-first authors.

https://doi.org/10.1016/j.scitotenv.2019.134414
0048-9697/© 2019 Elsevier B.V. All rights reserved.

et al., 1989; Zhitkovich, 2011). Due to its carcinogenicity, persistence, and bioaccumulation, chromium poses great risks to natural ecosystems and human health, and is hence listed as a priority environmental pollutant by the U.S. Environmental Protection Agency (USEPA) (Cefalu and Hu, 2004; Zayed and Terry, 2003). The maximum allowable concentration of total chromium in surface water and wastewater is 0.05 and 0.5 mg/L in China, and the maximum acceptable guideline concentration for total chromium in drinking water is 0.1 mg/L by USEPA (Lyu et al., 2017). The Cr(VI) concentrations in wastewater usually range from 30 to 200 mg/L (Fan et al., 2019). Hexavalent chromate (Cr(VI)) and trivalent forms (Cr(III)) are the primary species of chromium in the environment (Kotaś and Stasicka, 2000). Notably, Cr(VI) is firmly established as a carcinogen, especially with regard to human respiratory cancers. The higher solubility and mobility of Cr(VI) in water contribute to the higher carcinogenic and toxic effects of Cr(VI) on water safety and public health compared to that of Cr(III) (Costa and Klein, 2006; Zayed and Terry, 2003). Thus, it is critical to develop novel materials to facilitate efficient Cr(VI) adsorption and reduction for remediation strategies.

Biochar is a carbonaceous material produced by pyrolysis of organic biomass under relatively low temperature and oxygen-limited conditions (i.e., pyrolysis). Due to its smaller micropore volume, higher specific surface area, abundant functional groups and low cost, biochar has gained considerable attention for heavy metal and organic pollutant remediation (Li et al., 2019; Xiang et al., 2019; Yang et al., 2019). For example, Zhou et al. (2016) identified an adsorption-reduction mechanism for Cr(VI) interactions with ramie residue-derived biochar and concluded that Cr(VI) sorption resulted from reaction with the abundant carboxyl and hydroxyl groups on the biochar surface. The surface-adsorbed Cr (VI) was subsequently reduced to Cr(III) via ionic interaction with these polar functional groups on the biochar (Zhou et al., 2016). However, the pristine biochars, acquired from direct biomass pyrolysis, often have relatively low adsorptive and reductive ability for Cr(VI), but these properties are dependent on biomass feedstock and pyrolysis temperature (Dong et al., 2011; Jin et al., 2016; Zhang et al., 2018). Thus, specific activation processes, such as surface functionalization, molecular grafting, ultraviolet irradiation and ball milling, have been used to enhance the Cr(VI) removal performance of biochars (Peng et al., 2018; Zhang et al., 2019b; Zhao et al., 2017; Zhu et al., 2018b). These modifications not only increase surface adsorption sites, but also change surface charge and functional group characteristics that regulate Cr(VI) adsorption and reduction dynamics. Due to their nonmagnetic properties, pristine and modified biochars are difficult to separate from aqueous solutions after the reaction phase, thereby failing to achieve effective metal removal from the treated samples.

Iron-based materials, including iron oxides, zero-valent iron (ZVI) and iron sulfides, are ubiquitous and widely used for heavy metal remediation because of their high redox activity (Du et al., 2016; Gong et al., 2016; Huang et al., 2016; Li et al., 2016; Liu et al., 2019a). Due to their magnetic properties, iron-based materials can be easily separated from the aqueous phase with a magnet for subsequent regeneration and reuse (Graham and Bouwer, 2012; Wang and Lo, 2009). However, owing to their nano-size and magnetic interactions, iron-based materials are susceptible to agglomeration that leads to decreased mobility and lower remediation efficiency for Cr(VI). Consequently, there have been several attempts to load iron-based materials on biochar to decrease particle agglomeration and enhance remediation efficiency (Cho et al., 2019; Qian et al., 2017; Su et al., 2016; Sun et al., 2017; Sun et al., 2018; Sun et al., 2019; Zhu et al., 2018a). For example, ZVI was linked to the carbonaceous surface within the biochar pore network using chitosan as a dispersing and binding reagent (Zhou et al., 2014). It was found that the biochar/ZVI composites exhibited higher heavy metal removal efficiency through enhanced reduction and surface adsorption. Similarly, Han et al. (2016) concluded that Cr(VI) removal efficiency of magnetic biochar was 1–2 orders of magnitude higher than that of pristine biochar. Recently, $Fe_3O_4$ was used to increase the specific surface area and pore volume of magnetic biochar for Cr(VI) adsorption, as well as by promoting the generation of carbon-centered persistent free radicals (PFRs) for Cr(VI) reduction (Zhong et al., 2018). Notably, the Cr (VI) removal efficiency of magnetic biochar was highly correlated with the activated Fe(II) content in the composites (Yi et al., 2019).

Greigite ($Fe_3S_4$), containing reductive ferrous and sulfide, has been widely applied for pollutant remediation. Our previous studies demonstrated that magnetic $Fe_3S_4$ nanosheets induced roxarsone and Cr(VI) adsorption/reduction, and the roxarsone removal pathway was highly dependent on initial solution pH. The structural sulfides of $Fe_3S_4$ are reported to mediate ferric and chromium reduction by different processes (Liu et al., 2017; Liu et al., 2019b). Various carbonaceous compounds, such as $\beta$-cyclodextrin crystalline ($\beta$-CD), polyethylene glycol (PEG), cetyltrimethylammonium bromide (CTAB), polypyrrole (PPy), and reduced graphene oxide, have been used for surface functionalization of magnetic $Fe_3S_4$ to enhance heavy metal removal (Islam and Patel, 2017; Kong et al., 2017; Kong et al., 2015; Zhou et al., 2018). However, there are limited data regarding Cr(VI) reaction and removal potential using magnetic greigite/biochar composites.

Building upon previous research, we used rice husks (*Oryza sativa*) as the precursor of biochar to synthesize magnetic greigite/biochar composites (MGBs). The effects of greigite/biochar mass ratios and several operational variables (e.g., initial Cr(VI) and MGBs concentrations, solution pH, and inorganic ion competition) on Cr(VI) removal efficiency were investigated. Aqueous and surface chromium species, persistent free radical generation from biochar, and activated iron species were systematically investigated to determine chromium cycling dynamics.

## 2. Material and methods

### 2.1. Chemicals

Analytical-grade materials and solvents were purchased from Sinopharm (Shanghai, China): ferrous sulfate ($FeSO_4{\cdot}7H_2O$), *L*-cysteine ($C_3H_7NO_2S$), potassium dichromate ($K_2Cr_2O_7$), sulfuric acid ($H_2SO_4$), nitric acid ($HNO_3$), sodium hydroxide (NaOH), 1,5-diphenylcarbazide, 1,10-phenanthroline (Phen), sodium acetate ($CH_3COONa$), hydroxylamine hydrochloride ($NH_2OH{\cdot}HCl$), ethanol, ethylene glycol (EG), and acetone. All chemicals were used without further purification. Deionized water (>18 $M\Omega{\cdot}cm^{-1}$) was used for all experiments.

### 2.2. Synthesis of biochar and magnetic greigite/biochar composites (MGBs)

To prepare rice husk-derived biochar, washed and dried rice husk was pyrolyzed in a tube furnace (OTF1200X, Hefei Kejing Materials & Technology Co., Hefei, China) at 500 °C under oxygen-limited conditions by purging with $N_2$ gas (0.5 L/min) for 2 h (Wang et al., 2018a). The generated pristine biochar was naturally cooled to ambient temperature, ground and passed through a 100-mesh (149 μm) nylon sieve, and sequentially washed with deionized water and 0.1 mol/L HCl before drying at 90 °C. The generated biochar was stored in a sealed plastic tube until further use.

The magnetic greigite/biochar composites (MGBs) were synthesized using a solvothermal method with EG and *L*-cysteine as solvent and sulfur-source, respectively (Wang et al., 2018b; Zhang and Chen, 2009). In brief, 1.132 g $FeSO_4{\cdot}7H_2O$ was dissolved in

25 mL EG, then 1.0 g biochar was dispersed in the mixture under ultrasonication (15 min) to form a suspension solution (solution I). Then, 0.493 g *L*-cysteine was added to 25 mL EG to form solution II. Solution II was added dropwise to solution I within 5 min. The resulting suspension was transferred into a 100 mL Teflon-lined stainless steel autoclave and heated at 180 °C for 12 h. Upon cooling to room temperature, the resulting solid product was separated using a magnet and sequentially washed with deionized water and ethanol three times before drying overnight at 50 °C in a vacuum oven. The calculated mass ratio of greigite to biochar was 30% and the final product was denoted as MGB-30. For comparison, samples with greigite/biochar mass ratios of 20%, 10% and 5% were fabricated and referred to as MGB-20, MGB-10 and MGB-5, respectively.

### 2.3. Characterization

Powder X-ray diffraction (XRD) patterns of the as-prepared MGBs were recorded on a D8 Advance X-ray diffractometer (Bruker). Morphology and microstructure of MGBs were investigated by field emission scanning electron microscopy (FE-SEM, LEO 1450VP, Zeiss). The Brunauer-Emmett-Teller (BET) surface area was obtained using a Micromeritics ASAP 2460 system (Norcross). Fourier transform infrared spectrometry (FT-IR, Nicolet IS50, Thermo Scientific) was used to identify the surface function groups of MGBs at a resolution of 4 $cm^{-1}$ under ambient conditions. The surface potentials of MGBs were measured using a ZEN3690 Zetasizer (Malvern) at different pH values (1.4–11.0). High-resolution X-ray photoelectron spectroscopy (XPS) was used to determine surface elemental composition. Electron paramagnetic resonance (EPR) spectroscopy was applied to detect radicals associated with biochar and MGBs using a Bruker EPR E500 spectrometer (Bruker) under ambient conditions.

### 2.4. Experimental procedures

Cr(VI) removal experiments were conducted in 100 mL conical flasks using a batch methodology. The desired dosage of MGB powders and 50 mL Cr(VI) solution were sequentially added to the flask. To avoid photochemical reactions, flasks were covered with aluminum foil. The sample was shaken with a rotary shaker (SPH-100B, Shiping, China) at a constant speed of 150 rmp at 30 °C. The initial pH was adjusted with 0.1 mol/L of HCl or NaOH, and the final pH values were recorded with a Sartorius PB-10 pH meter. The dissolved fraction was separated from the suspension with a 0.22 μm polytetrafluoroethylene membrane filter at a regular time interval.

### 2.5. Analytical methods

The 1,5-diphenylcarbazide method was used to measure the dissolved Cr(VI) in aqueous solution (Mu et al., 2015). Total chromium ($Cr_{total}$) was determined with a PinAAcle 900 T flame atomic absorption spectrometer (FAAS, PerkinElmer). The difference between $Cr_{total}$ and Cr(VI) was considered the Cr(III) concentration. A modified 1,10-phenanthroline method was used to monitor the concentration of dissolved Fe(II) (Liu et al., 2015). The $Fe(phen)_3^{2-}$ complex was recorded at 510 nm with a UV-3101PC spectrophotometer (Shimadzu).

## 3. Results and discussion

### 3.1. Characterization of biochar and MGBs

Fig. 1a shows the XRD pattern of as-prepared biochar and MGBs. It reveals five intense characteristic peaks at 25.4°, 29.8°,

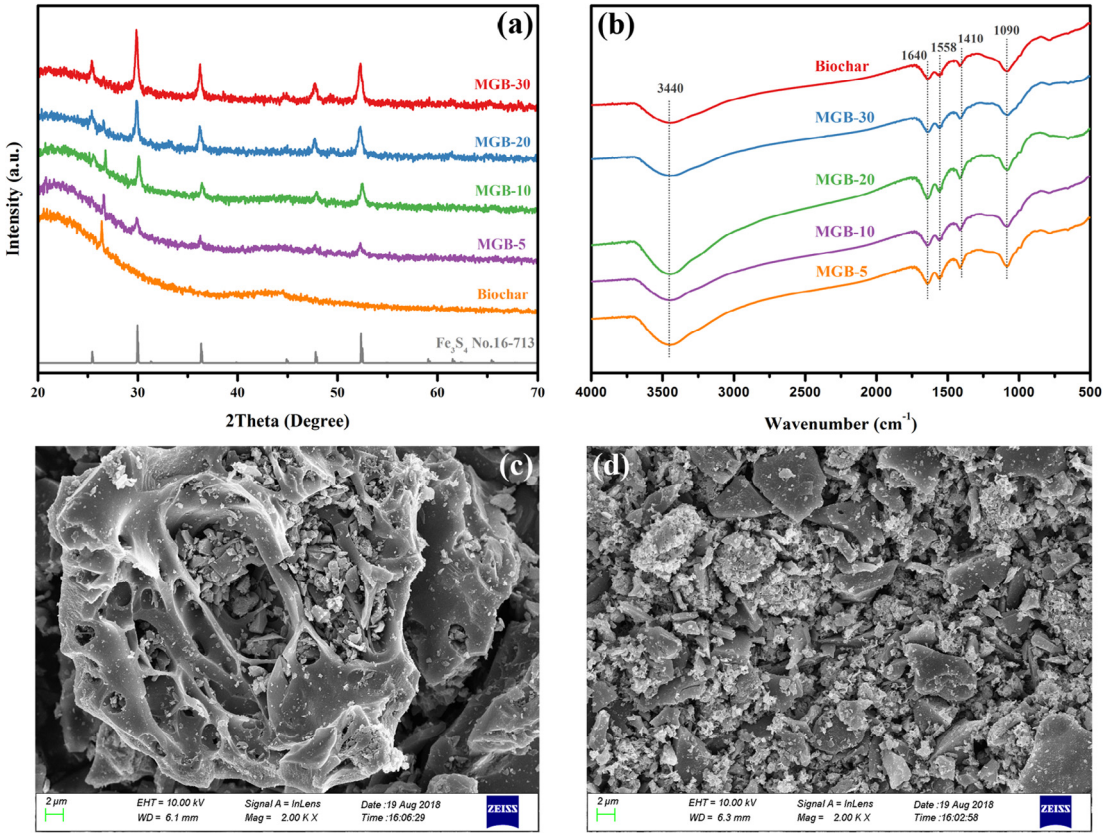


**Fig. 1.** Characterization of biochar and magnetic greigite/biochar composites: (a) XRD; (b) FT-IR; (c) SEM image of biochar; and (d) SEM image of MGB-30.

36.2°, 47.7° and 52.3° for MGBs that are attributable to the (220), (311), (400), (511) and (440) crystal faces of cubic greigite, respectively ($Fe_3S_4$, JCPDS card No. 16–713). Intensity of the specific diffraction peaks for $Fe_3S_4$ increased with increasing mass ratios of greigite/biochar, reflecting the higher $Fe_3S_4$ enrichment at higher ratios. Thus, it can be concluded that magnetic greigite/biochar composites were successfully prepared and $Fe_3S_4$ was well crystallized in the biochar matrix.

The surface functional groups of pristine biochar and MGBs identified by FTIR are shown in Fig. 1b. The wide band at ~3440 $cm^{-1}$ was assigned to the hydrogen-bonded O—H stretching vibration. Bands at 1640 and 1558 $cm^{-1}$ belong to the C=O stretching vibration from the oxygen-containing functional groups (Zhang et al., 2015). The bands at 1410 and 1090 $cm^{-1}$ were ascribed to the C—H stretching vibration of $-CH_2$ and the C—O stretching vibration of surface oxygen-containing functional groups, respectively (Zhang et al., 2019a). Absorption bands for pristine biochar and MGBs were similar, indicating limited changes to surface functional groups during the synthesis process of greigite/biochar composites.

The surface chemical compositions of biochar and MGB-30 were identified by XPS spectroscopy (Fig. S1). Total survey spectra revealed three specific peaks at 532, 400, and 284 eV, which correspond to O 1s, N 1s, and C 1s signals in the biochar and MGB-30. However, the signal intensity of MGB-30 was lower than that of pristine biochar, and new peaks occurred at 705–725 eV corresponding to Fe 2p resulting from modification of $Fe_3S_4$ on biochar. These results confirm that iron-based materials formed on the MGB-30 surface.

Morphology and microstructure of pristine biochar and magnetic greigite/biochar composite (MGB-30) are shown in Fig. 1c-d and S2. Pristine biochar displayed large scale structure (10s of microns) consisting of many formatted channels and internal macropores inherited from its intrinsic natural morphology/structure. By contrast, MGB-30 had an irregular microstructure with different shapes, and many flakes were aggregated to form a heterogeneous surface, suggesting the assembly of magnetic $Fe_3S_4$ on the biochar surface.

The $S_{BET}$ and average pore size of biochar were 165.9 $m^2 \cdot g^{-1}$ and 2.3 nm, respectively, confirming the porous structure of biochar

**Table 1**
BET surface area, average pore size, initial rate constant ($k_{Cr(VI)}$), and surface areas normalized initial rate constant ($k_{Cr(VI),\ surf}$) for biochar and MGBs. Initial concentrations of Cr (VI) and MGBs were 20 mg/L and 0. 8 g/L, respectively; Initial reaction pH values was 5.2.

| Sample | $S_{BET}$ ($m^2\ g^{-1}$) | Average pore size (nm) | $k_{Cr(VI)}$ ($min^{-1}$) | $k_{Cr(VI),\ surf}$ ($min^{-1} \cdot L \cdot m^{-2}$) |
|---|---|---|---|---|
| Biochar | 165.9 | 2.3 | – | – |
| MGB-30 | 17.6 | 10.2 | 0.059 ± 0.004 | 0.084 |
| MGB-20 | 15.2 | 11.6 | 0.020 ± 0.004 | 0.033 |
| MGB-10 | 10.2 | 13.1 | 0.004 ± 0.001 | 0.010 |
| MGB-5 | 14.0 | 10.2 | 0.001 ± 0.0001 | 0.002 |

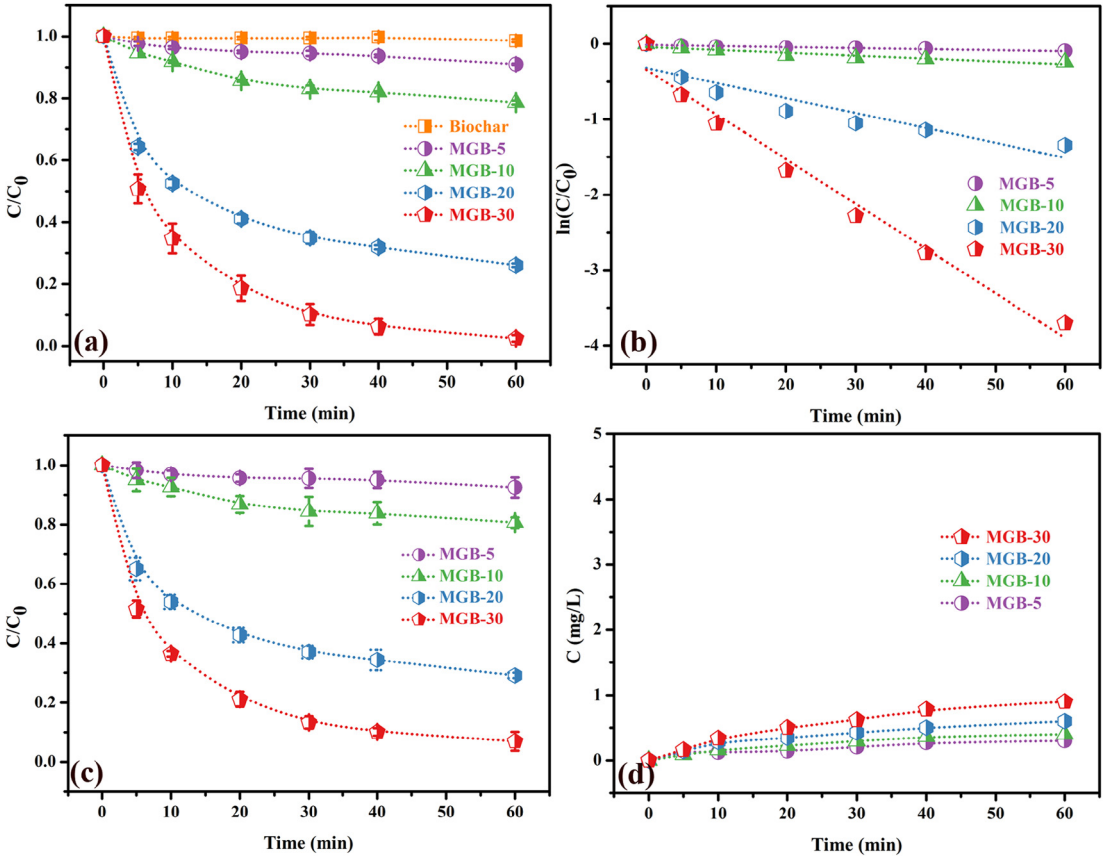


**Fig. 2.** (a) Time profiles of Cr(VI) removal with different materials. (b) Plots of $-\ln(C/C_0)$ versus time for Cr(VI) removal. (c) Time profiles for $Cr_{total}$ removal with MGBs. (d) Cr (III) concentrations generated during Cr(VI) removal process with MGBs. The initial concentrations of Cr(VI) and MGBs were 20 mg/L and 0.8 g/L, and the initial reaction pH values were 5.2, respectively.

(Table 1). These results are generally consistent with SEM observations (Figs. 1c and S2a–b). The $S_{BET}$ of MGBs sharply decreased (as low as 10–20 $m^2 \cdot g^{-1}$) and their average pore size increased (up to 10–13 nm) due to the collapse of the carbon skeleton and deposition of $Fe_3S_4$ on the biochar surface (Yang et al., 2017; Zhu et al., 2018).

Zeta potential of biochar and MGBs were variable over the investigated pH range of 1.4–11.0 (Fig. S3). Notably, the pristine biochar was negatively charged across the pH range from 2 to 11, owing to the dissociation of surface hydroxyl and carboxyl functional groups. In contrast, the surface potential changed to positive with addition of $Fe_3S_4$. The isoelectric point (IEP) increased from 4.5 to 6.6 as the greigite/biochar mass ratio increased from 5 to 30%. The positively charged surface of MGBs at lower pH values could favor adsorption of the negatively charged Cr(VI) species ($HCrO_4^-$) via electrostatic interaction (Fig. S4).

### 3.2. Cr(VI) removal by pristine biochar and MGBs

Pristine biochar removed very little Cr(VI) from aqueous solution within 60 min demonstrating its limited Cr(VI) adsorption capacity (Fig. 2a). In contrast, Cr(VI) removal efficiencies gradually increased from 9 to 98% with increasing mass ratios of greigite/biochar from 5 to 30%. All Cr(VI) removal processes by MGBs followed a pseudo-first-order kinetic equation (Fig. 2b). The apparent Cr(VI) removal rate constants ($k_{Cr(VI)}$) for MGB-5, MGB-10, MGB-20 and MGB-30 were $0.001 \pm 0.0001$, $0.004 \pm 0.001$, $0.020 \pm 0.004$ and $0.059 \pm 0.004$ $min^{-1}$, respectively (Table 1). Due to the potential effects of specific surface area on Cr(VI) removal efficiency by heterogeneous materials, we subsequently compared removal rate constants normalized for BTE-surface area ($k_{Cr(VI),\ surf}$). The $k_{Cr(VI),\ surf}$ of MGB-5, MGB-10, MGB-20 and MGB-30 were 0.002, 0.010, 0.033 and 0.084 $min^{-1} \cdot L \cdot m^{-2}$, respectively, which indicate that Cr (VI) removal by MGBs was ascribed to the higher $Fe_3S_4$ mass ratios rather than differences in surface area.

### 3.3. Chromium species distribution during the removal process with MGBs

Total chromium ($Cr_{total}$) in the aqueous phase was monitored during the Cr(VI) removal process by MGBs. Final $Cr_{total}$ concentrations decreased from 18.5 to 1.4 mg/L as the mass ratio of greigite/biochar increased from 5 to 30% (Fig. 2c). This indicates that $Cr_{total}$ removal efficiency was highly dependent on the $Fe_3S_4$ mass ratios loaded on the MGBs. The calculated maximum Cr adsorption capacity and maximum removal efficiency of MGB-30 was 23.25 mg/g and 93%, respectively, which was much higher than that of $Fe_3O_4$/Biochar (8.35 mg/g) (Zhong et al., 2018). Moreover, the concentration of $Cr_{total}$ was slightly higher than that of Cr(VI), demonstrating the generation of dissolved Cr(III). Calculated Cr (III) concentrations at 60 min were 0.301, 0.412, 0.634 and 0.902 mg/L in the presence of MGB-5, MGB-10, MGB-20 and MGB-30, respectively (Fig. 2d). This demonstrates that the higher ratio of $Fe_3S_4$ loaded on MGBs promoted greater Cr(VI) reduction. All of the Cr(III) concentrations were lower than 1 mg/L, which we ascribe to the limited solubility of Cr(III) under the experimental conditions. These results provide strong evidence for the Cr adsorption on the surface of MGBs.

XPS was used to examine surface structure information and elemental composition of MGB-30 before and after the Cr(VI) removal process (Fig. 3). The appearance of a typical Cr XPS peak was observed in the total survey spectra, indicating Cr adsorption/precipitation on the MGB-30 surface. Moreover, the three peaks at 576.8578.0, and 579.2 eV in the high-resolution spectra of Cr 2 are assigned to the Cr(III)-O, Cr(III)-OH and Cr(VI)-O of $Cr_2O_3$, Cr

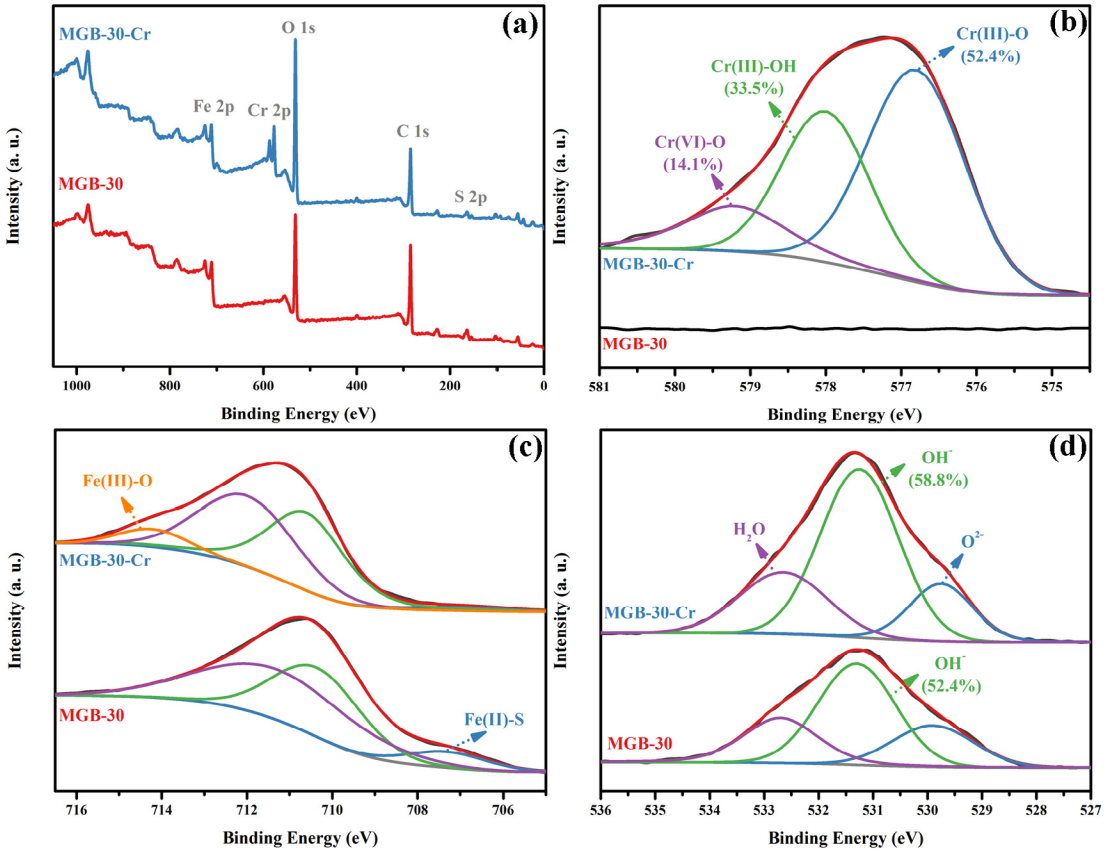


**Fig. 3.** XPS spectra of MGB-30 before and after Cr(VI) removal. (a) The total survey spectra; (b), (c) and (d) high resolution of Cr 2p, Fe 2p and O 1s, respectively.

$(OH)_3$ and $Cr_2O_7^{2-}$, respectively (Lyu et al., 2018). The higher relative fraction (85.9%) of Cr(III) suggested a significant contribution of Cr(VI) reduction rather than direct Cr(VI) adsorption. Moreover, the relative fractions of Cr(III)-O with MGB-20, MGB-10, and MGB-5 were higher than that of Cr(VI) (Fig. S5), indicating a significant Cr(VI) reduction pathway during Cr(VI) removal by MGBs.

High-resolution spectra of Fe 2p and O 1s were also examined to further elucidate the Cr(VI) removal process. Similar to our previous study (Liu et al., 2019b), the relative fraction of Fe(II)-S at 707.3 eV sharply decreased after Cr(VI) treatment, implying a significant interaction between Fe(II) and Cr(VI). Correspondingly, a new peak was found at a specific binding energy of 714.3 eV following Cr(VI) removal, suggesting the oxidation of Fe(II) to form Fe(III)-O. Moreover, the relative fraction of O 1s assigned to hydroxide (531.4 eV) increased from 52.4 to 58.8%, confirming the generation of Fe—Cr hydroxide on the MGB surface. Thus, we posit that Cr(VI) was adsorbed on the MGB-30 surface, and subsequently reduced to Cr (III) along with the corresponding oxidation of Fe(II).

As the generated Fe—Cr hydroxides may block further redox reactivity of MGBs, we separated the reacted MGBs from the suspension with a magnet and reused the material with no further chemical treatment for another round of Cr(VI) removal under the same conditions. The MGB-30 exhibited excellent magnetism and was easily separated from the solution with a magnet even after three reaction cycles (Fig. S6). However, Cr(VI) removal efficiencies decreased from 98% to 52% and 31% for the 2nd and 3rd reaction cycles, respectively (Fig. S7). This result was similar to our previous study of Cr(VI) removal using $Fe_3S_4$ (Liu et al., 2019b), and demonstrates the negative effects of the generated Fe—Cr hydroxides on further Cr(VI) removal. Following three reactions cycles, the MGB-30 was soaked in 1 mol/L of $HNO_3$ for 12 h to dissolve the surface Fe—Cr hydroxides and then used for a 4th reaction cycle. The Cr(VI) removal efficiency of the MGBs was restored to 73% after this simple reactivation step. The decrease in Cr(VI) removal efficiency between the 1st (98%) and 4th (73%) reaction cycles with regenerated MGB was attributed to incomplete dissolution of Fe—Cr hydroxides from the MGB surface by the dilute $HNO_3$.

### 3.4. Effects of environmental factors on Cr(VI) removal efficiency with MGBs

Cr(VI) removal efficiency is dependent on surface adsorption sites and reductive ability of heterogeneous materials, which are strongly affected by reactant dosage, solution pH, and co-existing ions. Thus, removal rates with initial Cr(VI) concentrations of 10–50 mg/L were examined. The Cr(VI) removal efficiency reached up to 80% within 20 min and gradually increased to 99% within 60 min at initial Cr(VI) concentrations of 10 to 20 mg/L (Fig. 4a). However, the removal efficiency significantly decreased when the initial Cr(VI) concentrations were increased from 30 to 50 mg/L. Due to the limited number of reactive sites for a fixed dosage of MGBs, low initial Cr(VI) concentration resulted in a higher ratio of reactive sites relative to Cr(VI) (Fu et al., 2015; Gong et al., 2017). In addition, high Cr(VI) concentrations enhance formation of Fe-(hydroxyl)oxide or sulfide precipitates on MGB surfaces reducing surface reactivity (Gong et al., 2017; Wu et al., 2018).

Subsequently, we evaluated Cr(VI) removal efficiency at MGBs dosages in the range of 0.2–0.8 g/L. Cr(VI) removal efficiency at a MGB-30 dosage of 0.2 g/L was only 22.4%, which may be limited by the lack of adsorption sites and reductive species at the low MGB concentration (Fig. 4b). Moreover, Cr(VI) removal efficiencies reached up to 98% and the $k_{Cr(VI)}$ increased from 0.004 to 0.059 $min^{-1}$ as MGB dosage increased to 0.8 g/L (Fig. S8). Higher dosages of MGB-30 provide additional adsorption sites, as well as promoting greater dissolution of iron sulfide loaded on the biochar.

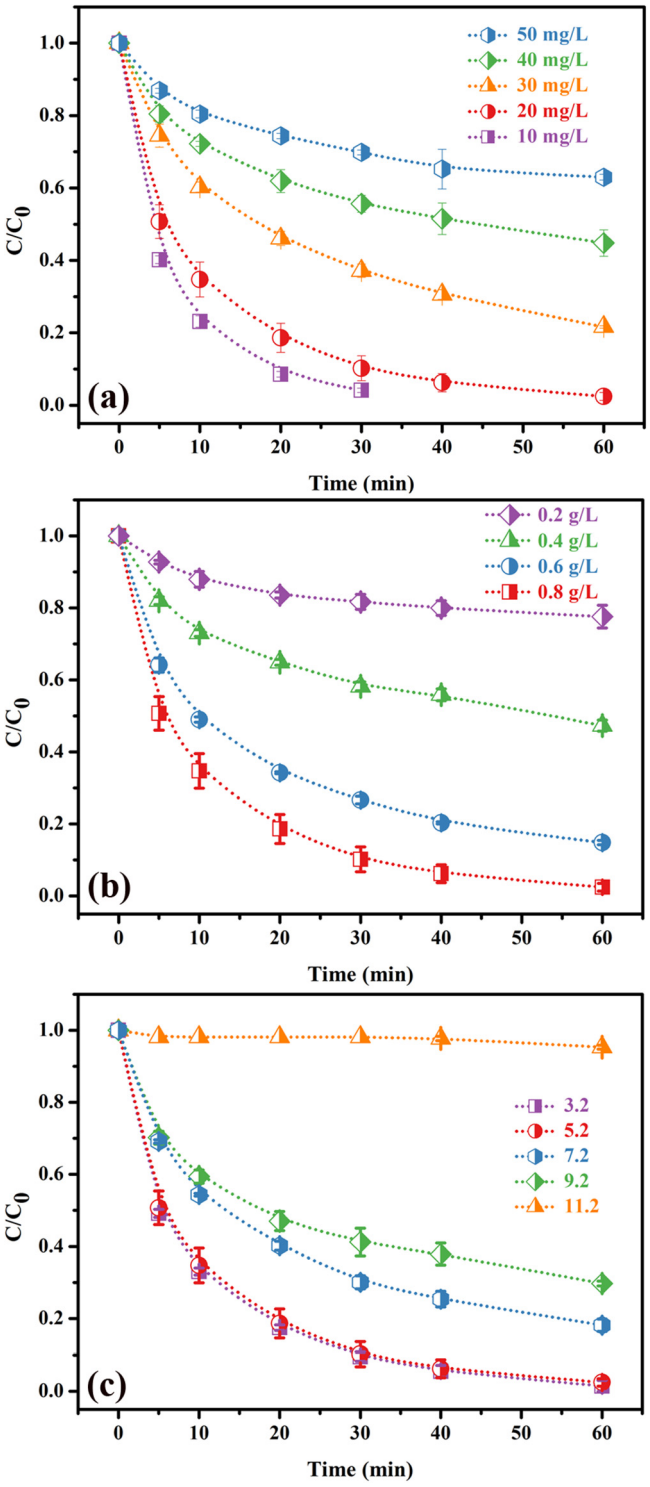


**Fig. 4.** Effects of (a) initial Cr(VI) concentration, (b) MGB-30 dosage, and (c) initial pH valued on Cr(VI) removal efficiency in the presence of MGB-30.

In natural aquatic environments, Cr(VI) coexists with several inorganic ions resulting in potential competitive interactions. Thus, we examined Cr(VI) removal processes with MGBs in matrices with 10 mg/L of NaCl, KCl, $CaCl_2$ and $MgCl_2$ solution. Common cations had limited effects on Cr(VI) removal efficiency, which was ascribed to the lack of competitive adsorption between Cr(VI) and cations (Fig. S9a). In comparison, Fig. S9b shows the effects of four common anions ($Cl^-$, $NO_3^-$, $CO_3^{2-}$, $SO_4^{2-}$) on the Cr(VI) removal process. All four anions had a slightly inhibitory effects on Cr(VI) removal efficien-

cies, and their influence followed the order: $Cl^- < NO_3^- < CO_3^{2-} < SO_4^{2-}$. These inhibitory effects likely result from the competitive adsorption dynamics between $Cr_2O_7^{2-}$ and the competing anions for positive charged sorption sites on MGBs (Zhang et al., 2015).

Cr(VI) removal efficiency with MGB-30 was further examined for initial pH values of 3.2–11.2 (Fig. 4c, Fig. S10). The $k_{Cr(VI)}$ slightly decreased from 0.066 to 0.059 $min^{-1}$ and then sharply decreased to 0.001 $min^{-1}$ as the initial solution pH increased from 3.2 to 5.2 and 11.2, respectively. These results indicate a significant effect of solution pH on Cr(VI) removal performance by MGBs. The Cr(VI) removal process is mediated by iron sulfides, which facilitate Cr (VI) reduction and/or adsorption in the aqueous phase and on the sulfide surface. When the initial pH (3.2–5.2) was less than $pH_{ZPC}$ (6.1), the MGB-30 surface was positively charged allowing adsorption of the negatively charge Cr(VI) ion to the MGB surface by direct electrostatic attraction. Additionally, the lower pH promotes the dissolution/oxidation of $Fe_3S_4$ to release ferrous ions that subsequently contribute to reduction of Cr(VI) in the aqueous phase. With increases of initial pH from 7.2 to 11.2, the MGB-30 surface became negatively charged, and the dominant Cr(VI) species ($CrO_4^{2-}$) was not adsorbed on MGB-30 via electrostatic attraction. Moreover, ferric ions are hydrolyzed/precipitated under alkaline conditions, which lower their contribution to Cr(VI) reduction.

Temperature is another crucial factor determining the mobility and transfer of molecules. Thus, we investigated Cr(VI) removal efficiency across the temperature range of 30–50 °C (Fig. S11). Cr (VI) was completely removed from the aqueous phase in the range of 30–50 °C and $k_{Cr(VI)}$ increased from 0.059 to 0.070 $min^{-1}$ as temperature increased from 30 to 50 °C. We posit that the higher temperature favored the diffusion of molecules, resulting in more frequent interactions between Cr(VI) and MGBs (Zhu et al., 2018a).

### 3.5. Cr(VI) reduction mechanism with MGBs

To explore the effects of ferrous ions on Cr(VI) dynamics, we first compared the Cr(VI) removal efficiency of MGB-30 with and without 1,10-phenanthroline (Phen). $Cr_{total}$ removal efficiency decreased to 55.9% within 60 min and its inhibitory ratio was up to 86.4% in the presence of Phen, suggesting a significant contribution of ferrous ions on the Cr(VI) removal process (Fig. S12). Subsequently, the concentration of ferrous ions released from magnetic greigite/biochar composites was systematically investigated in water or Cr(VI) solution (Fig. 5a and b). The dissolved Fe(II) concentrations in MGBs/$H_2O$ systems gradually increased with increasing reaction time. Final Fe (II) concentrations increased from 1.0 to 13.2 mg/L as the greigite/biochar mass ratio increased from 5 to 30%, indicating the dissolution/oxidation of $Fe_3S_4$ loaded on biochar. In contrast, Fe(II) concentrations in MGBs/Cr(VI) systems sharply increased to maximum values at 5 min and then gradually decreased within 60 min. However, all Fe(II) concentrations detected in MGBs/Cr(VI) systems were much lower than those of MGBs/$H_2O$ systems, confirming reactions between Cr(VI) and Fe(II) during the treatment process with magnetic greigite/biochar composites.

Corresponding to ferrous ion oxidation in the presence of Cr(VI), insoluble ferric ions are generated and precipitate on the surface of the heterogeneous materials, which then inhibited further Cr(VI) reduction (Gong et al., 2016). Thus, it is critical to consider the importance of the in situ Fe(III)/Fe(II) cycle for iron-based materials during Cr(VI) treatment processes. Next, we investigated Fe(III) reductive ability in the presence of pristine biochar and MGB-30. The concentration of added Fe(III) gradually decreased from 20 to 14.7 mg/L within 60 min, and the Fe(II) concentration correspondingly increased to 3.8 mg/L, suggesting the reduction of Fe(III) to Fe

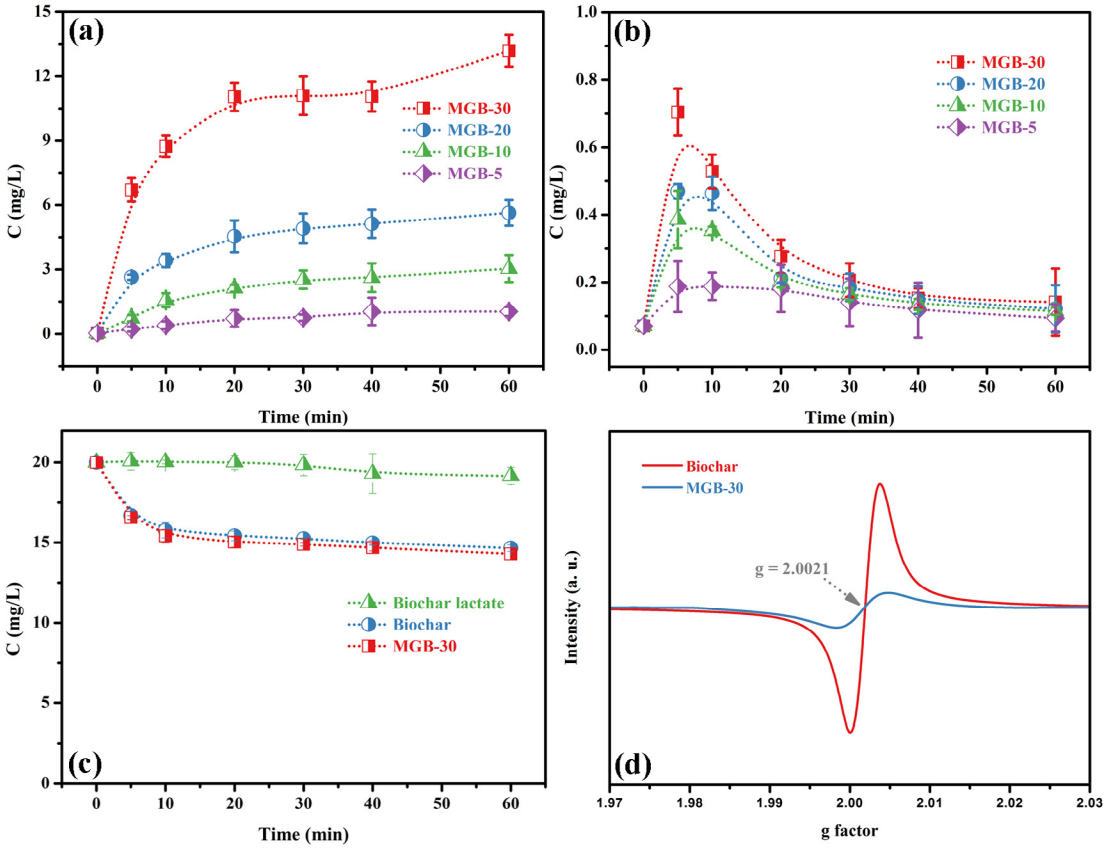


**Fig. 5.** (a) and (b) Time profiles of dissolved Fe(II) released from MGBs in the absence and presence of Cr(VI). (c) Time profiles of additional Fe(III) in the presence of biochar, biochar lactate and MGB-30, respectively. (d) EPR spectra of biochar and MBG-30. The initial concentrations of Cr(VI) and MGBs were 20 mg/L and 0.8 g/L, and the initial reaction pH values were 5.2, respectively.

(II) mediated by the pristine biochar (Figs. 5c and S13). To clarify the effects of dissolved and undissolved biochar on the reduction of Fe(III), the biochar lactate was fractionated from pristine biochar after 60 min and used to reduce Fe(III). It revealed that Fe(III) concentration was not depressed under the same conditions, ruling out direct Fe(III) reduction with dissolved biochar in aqueous solution. Moreover, the Fe(III) concentration in the MGB-30 system decreased from 20 to 14.3 mg/L with a corresponding increase in Fe(II) concentration to 15.7 mg/L, which was similar to that measured in the pristine biochar system. The Fe(II) concentrations were lower than the values (5.3 and 18.8 mg/L) calculated from Fe(III) reduction and MGB-30 dissolution, suggesting the partial adsorption/precipitation of Fe(II)/Fe(III) on the reactant surface. Although the structural sulfide in $Fe_3S_4$ could promote surface Fe (III)/Fe(II) cycling and induce Cr(VI) reduction (Liu et al., 2019b), its contribution was extremely low in this system, which may be caused by the lower ratio of $Fe_3S_4$ loaded on the composites and/or the higher reductive ability of biochar.

The abundance of carbon-centered persistent free radicals (PFRs) on carbonaceous materials can act as excellent reductants for pollutants and $H_2O_2$ activation (Ruan et al., 2019; Qin et al., 2018; Yang et al., 2016; Yu et al., 2019; Zhao et al., 2018; Zhong et al., 2018). Recently, Qin et al. (2017) demonstrated that PFRs on hydrothermal carbon could act as an electron donor and favor electron transfer from surface hydroxyl groups to Fe(III) to promote Fe(III)/Fe(II) cycling. Therefore, PFRs in pristine biochar and MGB-30 were quantified by EPR spectroscopy. The PFR intensity of MGB-30 was lower than that of pristine biochar suggesting the consumption of free radicals in the presence of $Fe_3S_4$ (Fig. 5d). Spectroscopic splitting factors (g-values) for both biochar and MGB-30 were 2.0021, which were close to the free electron g factor (2.0023). This indicates that PFRs have the properties of free electrons and can directly donate electrons to reduce the Fe(III) in $Fe_3S_4$. Based on these results, we posit that the carbon-centered PFRs on magnetic greigite/biochar composite surfaces accelerate electron transfer from biochar to Fe(III) ions to promote Fe(III)/Fe (II) cycling and subsequent enhancement of Cr(VI) removal.

## 4. Conclusions

A series of magnetic greigite/biochar composites with different mass ratios were synthesized using a solvothermal method and examined for their efficacy to remove Cr(VI) from wastewater. Cr (VI) removal efficiency depended on the mass ratio of $Fe_3S_4$/biochar, initial Cr(VI) and MGB concentrations, and solution pH. XPS and FAAS analyses indicated that the Cr(VI) treatment process was accompanied by coupled chromium adsorption and redox reactions. EPR spectra and Fe redox transformations revealed that high Cr(VI) removal efficiency with MGBs resulted from efficient Fe(III)/Fe(II) cycling via electron transfer from biochar to Fe(III) that was mediated by carbon-centered PFRs on MGBs. Overall, these results indicate that magnetic greigite/biochar composites have great potential for efficient removal of Cr(VI) from metal-polluted wastewaters.

## Declaration of Competing Interest

The authors declare that they have no conflict of interest in this paper.

## Acknowledgements

This work was jointly supported by the National Science Foundation of China (Grants 21707105, 21876125, and 41907106), Zhejiang Province Public Welfare Technology Application Research Project (Grants LGF18B070004 and LGF19B070009), Zhejiang Provincial Xinmiao Talent Project (Grant 2017R413033), and the Research and Development Fund of Wenzhou Medical University (Grant QTJ16013).

## Appendix A. Supplementary data

Supplementary data to this article can be found online at https://doi.org/10.1016/j.scitotenv.2019.134414.

## References

Cefalu, W.T., Hu, F.B., 2004. Role of chromium in human health and in diabetes. Diabetes Care 27, 2741–2751. https://doi.org/10.2337/diacare.27.11.2741.

Cho, D.W., Yoon, K., Ahn, Y., Sun, Y., Tsang, D.C.W., Hou, D., Ok, Y.S., Song, H., 2019. Fabrication and environmental applications of multifunctional mixed metal-biochar composites (MMBC) from red mud and lignin wastes. J. Hazard. Mater. 374, 412–419. https://doi.org/10.1016/j.jhazmat.2019.04.071.

Costa, M., Klein, C.B., 2006. Toxicity and carcinogenicity of chromium compounds in humans. Crit. Rev. Toxicol. 36, 155–163. https://doi.org/10.1080/10408440500534032.

Dong, X., Ma, L.Q., Li, Y., 2011. Characteristics and mechanisms of hexavalent chromium removal by biochar from sugar beet tailing. J. Hazard. Mater. 190, 909–915. https://doi.org/10.1016/j.jhazmat.2011.04.008.

Du, J., Bao, J., Lu, C., Werner, D., 2016. Reductive sequestration of chromate by hierarchical FeS@$Fe^0$ particles. Water Res. 102, 73–81. https://doi.org/10.1016/j.watres.2016.06.009.

Fan, Z., Zhang, Q., Gao, B., Li, M., Liu, C., Qiu, Y., 2019. Removal of hexavalent chromium by biochar supported nZVI composite: batch and fixed-bed column evaluations, mechanisms, and secondary contamination prevention. Chemosphere 217, 85–94. https://doi.org/10.1016/j.chemosphere.2018.11.009.

Fu, R., Yang, Y., Zhen, X., Zhang, X., Guo, X., Bi, D., 2015. The removal of chromium (VI) and lead (II) from groundwater using sepiolite-supported nanoscale zero-valent iron (S-NZVI). Chemoshpere 138, 726–734. https://doi.org/10.1016/j.chemosphere.2015.07.051.

Gong, Y.Y., Tang, J.C., Zhao, D.Y., 2016. Application of iron sulfide particles for groundwater and soil remediation: a review. Water Res. 89, 309–320. https://doi.org/10.1016/j.watres.2015.11.063.

Gong, Y., Gai, L., Tang, J., Fu, J., Wang, Q., Zeng, E.Y., 2017. Reduction of Cr(VI) in simulated groundwater by FeS-coated iron magnetic nanoparticles. Sci. Total Environ. 595, 743–751. https://doi.org/10.1016/j.scitotenv.2017.03.282.

Graham, A.M., Bouwer, E.J., 2012. Oxidative dissolution of pyrite surfaces by hexavalent chromium: surface site saturation and surface renewal. Geochim. Cosmochim. Acta 83, 379–396. https://doi.org/10.1016/j.gca.2012.01.006.

Han, Y., Cao, X., Ouyang, X., Sohi, S.P., Chen, J., 2016. Adsorption kinetics of magnetic biochar derived from peanut hull on removal of Cr (VI) from aqueous solution: effects of production conditions and particle size. Chemosphere 145, 336–341. https://doi.org/10.1016/j.chemosphere.2015.11.050.

Huang, X., Hou, X., Song, F., Zhao, J., Zhang, L., 2016. Facet-dependent Cr(VI) adsorption of hematite nanocrystals. Environ. Sci. Technol. 50, 1964–1972. https://doi.org/10.1021/acs.est.5b05111.

Islam, M., Patel, R., 2017. Solvothermal synthesis of greigite ($Fe_3S_4$)-conducting polypyrrole nanocomposite and its application towards arsenic removal. Sep. Sci. Technol. 52, 2837–2854. https://doi.org/10.1080/01496395.2017.1377247.

Jin, J., Li, Y., Zhang, J., Wu, S., Cao, Y., Liang, P., Zhang, J., Wong, M.H., Wang, M., Shan, S., Christie, P., 2016. Influence of pyrolysis temperature on properties and environmental safety of heavy metals in biochars derived from municipal sewage sludge. J. Hazard. Mater. 320, 417–426. https://doi.org/10.1016/j.jhazmat.2016.08.050.

Kimbrough, D.E., Cohen, Y., Winer, A.M., Creelman, L., Mabuni, C., 1999. A critical assessment of chromium in the environment. Crit. Rev. Environ. Sci. Technol. 29 (1), 1–46. https://doi.org/10.1080/10643389991259164.

Kong, L., Yan, L., Qu, Z., Yan, N., Li, L., 2015. $\beta$-Cyclodextrin stabilized magnetic $Fe_3S_4$ nanoparticles for efficient removal of Pb(II). J. Mater. Chem. A 3, 15755–15763. https://doi.org/10.1039/c5ta03442f.

Kong, L., Li, Z., Huang, X., Huang, S., Sun, H., Liu, M., Li, L., 2017. Efficient removal of Pb(II) from water using magnetic $Fe_3S_4$/reduced graphene oxide composites. J. Mater. Chem. A 5, 19333–19342. https://doi.org/10.1039/C7TA05389D.

Kotaś, J., Stasicka, Z., 2000. Chromium occurrence in the environment and methods of its speciation. Environ. Pollut. 107, 263–283. https://doi.org/10.1016/S0269-7491(99)00168-2.

Li, Y., Liang, J., He, X., Zhang, L., Liu, Y., 2016. Kinetics and mechanisms of amorphous $FeS_2$ induced Cr(VI) reduction. J. Hazard. Mater. 320, 216–225. https://doi.org/10.1016/j.jhazmat.2016.08.010.

Li, N., Yin, M., Tsang, D.C.W., Yang, S., Liu, J., Li, X., Song, G., Wang, J., 2019. Mechanisms of U(VI) removal by biochar derived from *Ficus microcarpa* aerial root: a comparison between raw and modified biochar. Sci. Total Environ. 697,. https://doi.org/10.1016/j.scitotenv.2019.134115 134115.

Liu, W., Wang, Y., Ai, Z., Zhang, L., 2015. Hydrothermal synthesis of $FeS_2$ as a high-efficiency Fenton reagent to degrade alachlor via superoxide-mediated Fe(II)/Fe (III) cycle. ACS Appl. Mater. Interfaces 7, 28534–28544. https://doi.org/10.1021/acsami.5b09919.

Liu, W., Ai, Z., Dahlgren, R.A., Zhang, L., Wang, X., 2017. Adsorption and reduction of roxarsone on magnetic greigite ($Fe_3S_4$): indispensable role of structural sulfide. Chem. Eng. J. 330, 1232–1239. https://doi.org/10.1016/j.cej.2017.07.176.

Liu, J., Li, N., Zhang, W., Wei, X., Tsang, D.C.W., Sun, Y., Luo, X., Bao, Z., Zheng, W., Wang, J., Xu, G., Hou, L., Chen, Y., Feng, Y., 2019a. Thallium contamination in farmlands and common vegetables in a pyrite mining city and potential health risks. Envion. Pollut. 248, 906–915. https://doi.org/10.1016/j.envpol.2019.02.092.

Liu, W., Jin, L., Xu, J., Liu, J., Li, Y., Zhou, P., Wang, C., Dahlgren, R.A., Wang, X., 2019b. Insight into pH dependent Cr(VI) removal with magnetic $Fe_3S_4$. Chem. Eng. J. 359, 564–571. https://doi.org/10.1016/j.cej.2018.11.192.

Lyu, H., Tang, J., Huang, Y., Gai, L., Zeng, E.Y., Liber, K., Gong, Y., 2017. Removal of hexavalent chromium from aqueous solutions by a novel biochar supported nanoscale iron sulfide composite. Chem. Eng. J. 322, 516–524. https://doi.org/10.1016/j.cej.2017.04.058.

Lyu, H., Zhao, H., Tang, J., Gong, Y., Huang, Y., Wu, Q., Gao, B., 2018. Immobilization of hexavalent chromium in contaminated soils using biochar supported nanoscale iron sulfide composite. Chemosphere 194, 360–369. https://doi.org/10.1016/j.chemosphere.2017.11.182.

Mu, Y., Ai, Z., Zhang, L., Song, F., 2015. Insight into core-shell dependent anoxic Cr (VI) removal with Fe@$Fe_2O_3$ nanowires: indispensable role of surface bound Fe (II). ACS Appl. Mater. Interfaces 7, 1997–2005. https://doi.org/10.1021/am507815t.

Peng, Z., Zhao, H., Lyu, H., Wang, L., Huang, H., Nan, Q., Tang, J., 2018. UV modification of biochar for enhanced hexavalent chromium removal from aqueous solution. Environ. Sci. Pollut. Res. 25, 10808–10819. https://doi.org/10.1007/s11356-018-1353-3.

Qian, L., Zhang, W., Yan, J., Han, L., Chen, Y., Ouyang, D., Chen, M., 2017. Nanoscale zero-valent iron supported by biochars produced at different temperatures: synthesis mechanism and effect on Cr(VI) removal. Environ. Pollut. 223, 153–160. https://doi.org/10.1016/j.envpol.2016.12.077.

Qin, Y., Zhang, L., An, T., 2017. Hydrothermal carbon-mediated Fenton-like reaction mechanism in the degradation of alachlor: direct electron transfer from hydrothermal carbon to Fe(III). ACS Appl. Mater. Interfaces 9, 17115–17124. https://doi.org/10.1021/acsami.7b03310.

Qin, Y., Li, G., Gao, Y., Zhang, L., Ok, Y.S., An, T., 2018. Persistent free radicals in carbon-based materials on transformation of refractory organic contaminants (ROCs) in water: a critical review. Water Res. 137, 130–143. https://doi.org/10.1016/j.watres.2018.03.012.

Rai, D., Eary, L.E., Zachara, J.M., 1989. Environmental chemistry of chromium. Sci. Total Environ. 86, 15–23. https://doi.org/10.1016/0048-9697(89)90189-7.

Ruan, X., Sun, Y., Du, W., Tang, Y., Liu, Q., Zhang, Z., Doherty, W., Frost, R.L., Qian, G., Tsang, D.C.W., 2019. Formation, characteristics, and applications of environmentally persistent free radicals in biochars: a review. Bioresour. Technol. 281, 457–468. https://doi.org/10.1016/j.biortech.2019.02.105.

Su, H., Fang, Z., Tsang, P.E., Fang, J., Zhao, D., 2016. Stabilisation of nanoscale zero-valent iron with biochar for enhanced transport and in-situ remediation of hexavalent chromium in soil. Environ. Pollut. 214, 94–100. https://doi.org/10.1016/j.envpol.2016.03.072.

Sun, Y., Lei, C., Khan, E., Chen, S.S., Tsang, D.C.W., Ok, Y.S., Lin, D., Feng, Y., Li, X., 2017. Nanoscale zero-valent iron for metal/metalloid removal from model hydraulic fracturing wastewater. Chemosphere 176, 315–323. https://doi.org/10.1016/j.chemosphere.2017.02.119.

Sun, Y., Lei, C., Khan, E., Chen, S.S., Tsang, D.C.W., Ok, Y.S., Lin, D., Feng, Y., Li, X., 2018. Aging effects on chemical transformation and metal(loid) removal by entrapped nanoscale zero-valent iron for hydraulic fracturing wastewater treatment. Sci. Total Environ. 615, 498–507. https://doi.org/10.1016/j.scitotenv.2017.09.332.

Sun, Y., Yu, I.K.M., Tsang, D.C.W., Cao, X., Lin, D., Wang, L., Graham, N.J.D., Alessi, D.S., Komarek, M., Ok, Y.S., Feng, Y., Li, X.D., 2019. Multifunctional iron-biochar composites for the removal of potentially toxic elements, inherent cations, and hetero-chloride from hydraulic fracturing wastewater. Environ. Int. 124, 521–532. https://doi.org/10.1016/j.envint.2019.01.047.

Wang, P., Lo, I.M., 2009. Synthesis of mesoporous magnetic gamma-$Fe_2O_3$ and its application to Cr(VI) removal from contaminated water. Water Res. 43, 3727–3734. https://doi.org/10.1016/j.watres.2009.05.041.

Wang, S., Guo, W., Gao, F., Wang, Y., Gao, Y., 2018a. Lead and uranium sorptive removal from aqueous solution using magnetic and nonmagnetic fast pyrolysis rice husk biochars. RSC Adv. 8, 13205–13217. https://doi.org/10.1039/C7RA13540H.

Wang, Y., Wang, J., Deng, R., Xv, S., Lv, X., Zhou, J., Li, S., Cao, F., Qin, G., 2018b. Preparation and photocatalytic property of porous $\alpha$-$Fe_2O_3$ nanoflowers. Mater. Res. Bull. 107, 94–99. https://doi.org/10.1016/j.materresbull.2018.07.013.

Wu, B., Peng, D., Hou, S., Tang, B., Wang, C., Xu, H., 2018. Dynamic study of Cr(VI) removal performance and mechanism from water using multilayer material coated nanoscale zerovalent iron. Environ. Pollut. 240, 717–724. https://doi.org/10.1016/j.envpol.2018.04.099.

Xiang, Y., Xu, Z., Wei, Y., Zhou, Y., Yang, X., Yang, Y., Yang, J., Zhang, J., Luo, L., Zhou, Z., 2019. Carbon-based materials as adsorbent for antibiotics removal: mechanisms and influencing factors. J. Environ. Manag. 237, 128–138. https://doi.org/10.1016/j.jenvman.2019.02.068.

Yang, J., Pan, B., Li, H., Liao, S., Zhang, D., Wu, M., Xing, B., 2016. Degradation of *p*-nitrophenol on biochars: role of persistent free radicals. Environ. Sci. Technol. 50, 694–700. https://doi.org/10.1021/acs.est.5b04042.

Yang, F., Zhang, W., Li, J., Wang, S., Tao, S., Wang, Y., Zhang, Y., 2017. The enhancement of atrazine sorption and microbial transformation in biochars amended black soils. Chemosphere 189, 507–516. https://doi.org/10.1016/j.chemosphere.2017.09.022.

Yang, X., Wan, Y., Zheng, Y., He, F., Yu, Z., Huang, J., Wang, H., Ok, Y.S., Jiang, Y., Gao, B., 2019. Surface functional groups of carbon-based adsorbents and their roles in the removal of heavy metals from aqueous solutions: a critical review. Chem. Eng. J. 366, 608–621. https://doi.org/10.1016/j.cej.2019.02.119.

Yi, Y., Tu, G., Zhao, D., Tsang, P.E., Fang, Z., 2019. Biomass waste components significantly influence the removal of Cr(VI) using magnetic biochar derived from four types of feedstocks and steel pickling waste liquor. Chem. Eng. J. 360, 212–220. https://doi.org/10.1016/j.cej.2018.11.205.

Yu, J., Zhu, Z., Zhang, H., Chen, T., Qiu, Y., Xu, Z., Yin, D., 2019. Efficient removal of several estrogens in water by Fe-hydrochar composite and related interactive effect mechanism of $H_2O_2$ and iron with persistent free radicals from hydrochar of pinewood. Sci. Total Environ. 658, 1013–1022. https://doi.org/10.1016/j.scitotenv.2018.12.183.

Zayed, A.M., Terry, N., 2003. Chromium in the environment: factors affecting biological remediation. Plant Soil 249, 139–156. https://doi.org/10.1023/A:1022504826342.

Zhang, Z.J., Chen, X.Y., 2009. Magnetic greigite ($Fe_3S_4$) nanomaterials: shape-controlled solvothermal synthesis and their calcination conversion into hematite ($\alpha$-$Fe_2O_3$) nanomaterials. J. Alloy. Compd. 488, 339–345. https://doi.org/10.1016/j.jallcom.2009.08.127.

Zhang, M.M., Liu, Y.G., Li, T.T., Xu, W.H., Zheng, B.H., Tan, X.F., Wang, H., Guo, Y.M., Guo, F.Y., Wang, S.F., 2015. Chitosan modification of magnetic biochar produced from *Eichhornia crassipes* for enhanced sorption of Cr(VI) from aqueous solution. RSC Adv. 5, 46955–46964. https://doi.org/10.1039/c5ra02388b.

Zhang, X., Fu, W., Yin, Y., Chen, Z., Qiu, R., Simonnot, M.O., Wang, X., 2018. Adsorption-reduction removal of Cr(VI) by tobacco petiole pyrolytic biochar: batch experiment, kinetic and mechanism studies. Bioresour. Technol. 268, 149–157. https://doi.org/10.1016/j.biortech.2018.07.125.

Zhang, L., Fu, F., Tang, B., 2019a. Adsorption and redox conversion behaviors of Cr (VI) on goethite/carbon microspheres and akaganeite/carbon microspheres composites. Chem. Eng. J. 356, 151–160. https://doi.org/10.1016/j.cej.2018.08.224.

Zhang, Q.R., Wang, J.M., Lyu, H.H., Zhao, Q., Jiang, L.S., Liu, L., 2019b. Ball-milled biochar for galaxolide removal: sorption performance and governing mechanisms. Sci. Total Environ. 659, 1537–1545. https://doi.org/10.1016/j.scitotenv.2019.01.005.

Zhao, N., Zhao, C., Lv, Y., Zhang, W., Du, Y., Hao, Z., Zhang, J., 2017. Adsorption and coadsorption mechanisms of Cr(VI) and organic contaminants on $H_3PO_4$ treated biochar. Chemosphere 186, 422–429. https://doi.org/10.1016/j.chemosphere.2017.08.016.

Zhao, N., Yin, Z., Liu, F., Zhang, M., Lv, Y., Hao, Z., Pan, G., Zhang, J., 2018. Environmentally persistent free radicals mediated removal of Cr(VI) from highly saline water by corn straw biochars. Bioresour. Technol. 260, 294–301. https://doi.org/10.1016/j.biortech.2018.03.116.

Zhitkovich, A., 2011. Chromium in drinking water: sources, metabolism, and cancer risks. Chem. Res. Toxicol. 24, 1617–1629. https://doi.org/10.1021/tx200251t.

Zhong, D., Zhang, Y., Wang, L., Chen, J., Jiang, Y., Tsang, D.C.W., Zhao, Z., Ren, S., Liu, Z., Crittenden, J.C., 2018. Mechanistic insights into adsorption and reduction of hexavalent chromium from water using magnetic biochar composite: key roles of $Fe_3O_4$ and persistent free radicals. Environ. Pollut. 243, 1302–1309. https://doi.org/10.1016/j.envpol.2018.08.093.

Zhou, Y., Gao, B., Zimmerman, A.R., Chen, H., Zhang, M., Cao, X., 2014. Biochar-supported zerovalent iron for removal of various contaminants from aqueous solutions. Bioresour. Technol. 152, 538–542. https://doi.org/10.1016/j.biortech.2013.11.021.

Zhou, L., Liu, Y., Liu, S., Yin, Y., Zeng, G., Tan, X., Hu, X., Hu, X., Jiang, L., Ding, Y., Liu, S., Huang, X., 2016. Investigation of the adsorption-reduction mechanisms of hexavalent chromium by ramie biochars of different pyrolytic temperatures. Bioresour. Technol. 218, 351–359. https://doi.org/10.1016/j.biortech.2016.06.102.

Zhou, Y., Zhao, Y., Wu, X., Yin, W., Hou, J., Wang, S., Feng, K., Wang, X., 2018. Adsorption and reduction of hexavalent chromium on magnetic greigite ($Fe_3S_4$)-CTAB: leading role of Fe(II) and S(-II). RSC Adv. 8, 31568–31574. https://doi.org/10.1039/C8RA06534A.

Zhu, H., Tan, X., Tan, L., Chen, C., Alharbi, N.S., Hayat, T., Fang, M., Wang, X., 2018. Biochar derived from sawdust embedded with molybdenum disulfide for highly selective removal of $Pb^{2+}$. ACS Appl. Nano Mater. 1, 2689–2698. https://doi.org/10.1021/acsanm.8b00388.

Zhu, S., Huang, X., Wang, D., Wang, L., Ma, F., 2018a. Enhanced hexavalent chromium removal performance and stabilization by magnetic iron nanoparticles assisted biochar in aqueous solution: mechanisms and application potential. Chemosphere 207, 50–59. https://doi.org/10.1016/j.chemosphere.2018.05.046.

Zhu, Y., Li, H., Zhang, G., Meng, F., Li, L., Wu, S., 2018b. Removal of hexavalent chromium from aqueous solution by different surface-modified biochars: acid washing, nanoscale zero-valent iron and ferric iron loading. Bioresour. Technol. 261, 142–150. https://doi.org/10.1016/j.biortech.2018.04.004.